

An Improved Dynamical Model for the Microquasar XTE J1550-564[†]

Jerome A. Orosz

Department of Astronomy, San Diego State University, 5500 Campanile Drive, San Diego, CA 92182-1221

`orosz@sciences.sdsu.edu`

James F. Steiner, Jeffrey E. McClintock, Manuel A. P. Torres

Harvard-Smithsonian Center for Astrophysics, 60 Garden Street, Cambridge, MA 02138

`jsteiner@cfa.harvard.edu`, `jem@cfa.harvard.edu`, `mtorres@cfa.harvard.edu`

Ronald A. Remillard

Kavli Institute for Astrophysics and Space Research, Massachusetts Institute of Technology, Cambridge, MA 02139-4307

`rr@space.mit.edu`

Charles D. Bailyn

Department of Astronomy, Yale University, P.O. Box 208101, New Haven, CT 06520

`charles.bailyn@yale.edu`

Jon M. Miller

Department of Astronomy, University of Michigan, 500 Church Street, Dennison 814, Ann Arbor, MI 48109-1090

`jonmm@umich.edu`

ABSTRACT

We present an improved dynamical model of the X-ray binary and microquasar XTE J1550-564 based on new moderate-resolution optical spectroscopy and near-infrared photometry obtained with the 6.5m Magellan Telescopes at Las Campanas Observatory. Twelve spectra of the source were obtained using the Magellan Echellette Spectrograph between 2008 May 6 and August 4. In addition, several hundred images of the field were obtained between 2006 May and 2009 July in the J and K_S filters using the PANIC camera. The agreement between the 2006/2007 and 2008 J and K_S light curves is not perfect, and the differences can plausibly be attributed to a hot spot on the accretion disk during the 2006/2007 observations. By combining our new radial velocity measurements with previous measurements obtained 2001 May at the 8.2m VLT and with light curves, we find an orbital period of $P = 1.5420333 \pm 0.0000024$ days and a radial velocity semiamplitude of $K_2 = 363.14 \pm 5.97$ km s⁻¹, which together imply an optical mass function of $f(M) = 7.65 \pm 0.38 M_\odot$. We find that the projected rotational velocity of the secondary star is 55 ± 5 km s⁻¹, which implies a very extreme mass ratio of $Q \equiv M/M_2 \approx 30$.

[†]This paper includes data gathered with the 6.5 meter Magellan Telescopes located at Las Campanas Observatory, Chile.

Using a model of a Roche lobe-filling star and an azimuthally symmetric accretion disk, we fit simultaneously optical light curves from 2001, near-infrared light curves from 2008 and all of the radial velocity measurements to derive system parameters. We find an inclination of $74.7 \pm 3.8^\circ$ and component masses of $M_2 = 0.30 \pm 0.07 M_\odot$ and $M = 9.10 \pm 0.61 M_\odot$ for the secondary star and black hole, respectively. We note that these results depend on the assumption that in 2008, the disk does not have a hot spot, and that the fraction of light contributed by the accretion disk did not change between the spectroscopic and photometric observations. By considering two measured values of the disk fraction and by modeling various combinations of NIR and optical light curves, we show that our adopted black hole mass is probably not seriously in error, where the black hole mass ranges between $M = 8.91 \pm 1.10 M_\odot$ and $M = 13.94 \pm 1.64 M_\odot$. The radius of the secondary star for the adopted model is $1.75 \pm 0.12 R_\odot$. Using this radius, the average K_S magnitude, and an extinction of $A_K = 0.507 \pm 0.050$ mag, we find a distance of $4.38^{+0.58}_{-0.41}$ kpc, which is in good agreement with a recent distance estimate based on HI absorption lines.

1. Introduction

With the sole exception of Cygnus X-1, all of the 18 confirmed stellar black holes in the Galaxy are transient X-ray sources (Remillard & McClintock 2006). One of the most important and thoroughly-studied of these transient X-ray binary systems is XTE J1550–564 (hereafter J1550), which was discovered on 1998 September 6 (Smith et al. 1998). Within a week, its intensity rose to ~ 1.5 Crab, and on September 19–20, the source produced an impulsive and unprecedented flare that reached a peak intensity of 6.8 Crab (Sobczak et al. 2000). Following this remarkable $\lesssim 2$ -day event, the source returned to its pre-flare intensity and remained at that level for a month before fading to a state of near-obscurity. Remarkably, in early December the source again brightened. Within a few weeks thereafter, it reached an intensity of ~ 2.5 Crab and maintained that level for a few months before it slipped below the threshold of *RXTE* (a few mCrab) in mid-1999 (Sobczak et al. 2000). A second and smaller outburst was observed during 2000 April–June (Rodriguez et al. 2003), and three subsequent, brief mini-outbursts were observed in 2001, 2002, and 2003 (Remillard & McClintock 2006).

The source J1550 is especially important because of the relativistic phenomena it has exhibited. It is one of seven sources of high-frequency quasi-periodic oscillations (QPOs), and it is only one of four such sources that exhibit harmonic pairs of frequencies in a 3:2 ratio (Miller et al. 2001; Remillard et al. 2002a; Remillard & McClintock 2006). J1550 is also one of only three sources that has been observed to produce a large-scale relativistic X-ray jet (Corbel et al. 2002). This two-sided jet, observed in 2000 and 2002 by *Chandra*, was presumably launched during the powerful 1998 X-ray flare, which was observed to be accompanied by a superluminal radio jet (Hannikainen et al. 2009). The rich X-ray timing phenomenology of J1550 has also been important for studying the complex power spectra of black hole transients, which are often punctuated by strong low-frequency QPOs (Homan et al. 2001; Remillard et al. 2002b).

The optical counterpart of J1550 was identified shortly after the discovery of the X-ray source (Orosz et al. 1998) and extensive photometric observations were made during both the 1998–1999 and 2000 outburst cycles (Jain et al. 1999, 2001a,b). In May and June of 2001, in a state of deep quiescence, with the X-ray source dimmed by more than a million-fold (Corbel et al. 2006), we made optical photometric and spectroscopic observations of the counterpart (Orosz et al. 2002). The analysis of these data yielded a large mass function, $f(M) = 6.86 \pm 0.71 M_\odot$, thereby clinching the argument that the compact primary is a black hole. The dynamical model we developed is comprised of an $\approx 10 M_\odot$ black hole in a 1.54-day orbit with a late G or

early K companion.

In this paper, we revisit our earlier model, bringing to bear extensive near-infrared photometric data obtained during 2006–2009 and 12 echelle spectra obtained in 2008. These spectra have a resolving power $R = 4200 - 4950$, more than twice the resolving power of the spectra we used in our earlier analysis and modeling. In Orosz et al. (2002), using the low-resolution spectra available to us then, we adopted for the projected rotational velocity of the companion star the “tentative value of $V_{\text{rot}} \sin i = 90 \pm 10 \text{ km s}^{-1}$.” Now, using our higher-resolution spectra, we find $V_{\text{rot}} \sin i = 55 \pm 5 \text{ km s}^{-1}$. The effect of this new determination of the rotational velocity is to very significantly boost the mass ratio $Q \equiv M/M_2$ from ~ 9 to ~ 30 . This change accounts for most of the differences between the current model and our earlier one.

In Section 2, we present our new near-infrared light curves and our moderate resolution spectra. In Section 3 we discuss the analysis of the new data and the results we derive from them. In Section 4 we briefly discuss some of the implications for our results, and in Section 5 we end with a brief summary.

2. Observations and Reductions

2.1. Photometry

J1550 was observed in the near-infrared (NIR) using the Persson’s Auxiliary Nasmyth Infrared Camera (PANIC; Martini et al. 2004) and J , H , and K_S filters on the Magellan Baade telescope at Las Campanas Observatory. These data were obtained over runs spanning three years ranging from 2006 May to 2009 July. The data were primarily gathered in two observing sequences during 2007 May and 2008 April (see Table 1 for details). To mitigate problems inherent in the NIR arising from hot or dead pixels, the data were collected in sequences consisting of a “dice-5” dithering pattern with an offset between 6 and 8 arcseconds, with one or three exposures taken at each position. Each such group of observations have been combined for analysis using an IRAF reduction package for the PANIC detector, after being flat-fielded. In order to stay within the linear range of the detector, individual exposures were typically limited to 10s for all three bands. Dice-5 dithering sequences then are mostly either 50 or 150s in effective duration. In addition, a few sequences with exposure times of 3s were obtained in order to keep bright comparison stars in the linear regime.

We used the PANIC reduction package to perform the reductions on the images. While reducing the PANIC data, it was necessary to skip the default pipeline sky subtraction step. This step is designed to produce a blank sky image using a pixel-by-pixel median along a sequence of images. However, for crowded fields such as that of J1550, this sky image actually can inadvertently contain stars and other pattern noise. By omitting this step, the final images contained a low-level, large-scale curvature in sky brightness over the field. This effect had negligible impact on the psf-derived photometry.

All images were corrected for spatial distortion and nonlinearity and rotated and aligned to a common orientation. The highest quality data were stacked and combined to produce a deep field image from which a catalogue of field stars was derived. This list was used to uniformly analyze all images with the DAOPHOT (Stetson 1987) package in IRAF. Iterative selection produced approximately forty stars ranging from 1.0-4.5 mag brighter than J1550 with no signs of variability. These stars were used to calibrate the field by employing the least-squares differential photometric solution discussed in Honeycutt (1992).

Zero-point calibrations were derived using a set of 12 relatively isolated field stars with available 2MASS (Skrutskie et al. 2006) photometry, filtered to remove any clearly variable objects. The 2MASS magnitudes

were transformed to the LCO standard system following Carpenter (2001). These stars range from $\approx 12.5 - 14.5$ mag in K_S and $\approx 13 - 15$ mag in J . A weighted average based upon 2MASS uncertainties was used to determine the zero-point offsets, with total uncertainty estimated from a quadrature sum of the weighted error combined with a $\approx 1\%$ error describing the 2MASS field-to-field piecewise zero-point variability¹. The resultant uncertainties are 0.022, 0.019, and 0.019 mag in the J , H , and K_S -bands, respectively. The field near J1550 is relatively crowded (Figure 1). In particular, there are two stars close to J1550 on the sky: A star dubbed “A” that is about 25% as bright as J1550 and is located about 1 arcsecond to the northeast, and a star dubbed “B” that is only 5-10% as bright as J1550 and is about 0.7 arcseconds to the southeast. Because DAOPHOT had a high failure rate to solve for both J1550 and B, B was omitted from the DAOPHOT’s input star list. In order to assess any distortion in the derived magnitudes due to the proximity of A and B, a set of 2500 simulated fields in J and K_S were produced with the average noise and background level of a typical dice-5 sequence using an average brightness of J1550. Stars A and B, along with reference stars for calibration, were also included in the simulation. These simulations were analyzed in the same manner as the data. The scaling and position of the stars were iterated and adjusted until close ($\lesssim 2\%$) agreement was achieved between the average counts from a stack of 100 simulated images compared to a stack of 25 data images at comparable and good seeing ($\lesssim 0''.5$). The simulations uniformly sampled a range of seeing from FWHM $\approx 0''.35 - 2''.0$, a broader range than that spanned by the data. A step-like shift of ~ 0.05 mag appeared in the derived magnitude when the seeing became comparable to the point-separation of J1550 and B (see Figure 2). These simulations were also used to derive a seeing cut at $\approx 1''.2$, the confusion limit between J1550 and A.

This step-like impact on the J1550 light curves by contamination from B is well-described by a logistic curve of the form

$$\Delta = a + \frac{b}{1 + \exp[-(x - c)/d]}, \quad (1)$$

where the variable x is the seeing FWHM. This was fit to the simulations, achieving a goodness-of-fit of $\chi^2/\nu \approx 1.2$ for both J and K_S -bands. Seeing-based corrections for the data have been derived from these models and applied, scaling by the inverse of the observed flux (relative to band average). The corrections are typically 1%-2% and 5% at maximum. The uncertainty from this correction is small ($\sim 1\%$) and has been estimated and added in quadrature to the measurement errors. The H -band data were too sparse to derive a comparable phase-averaged correction. However, the noise and background level for H was very close to K_S , and so the K_S model was also used to correct the H -band data. (Note that the difference between J and K_S corrections is $\lesssim 1\%$ over the range of useful data, so any systematic effect from the use of a K_S -band model will be very small.)

For the final adopted light curves, data were screened to fulfill three conditions: (1) the seeing FWHM had to be $< 1''.2$, which led to the rejection of 5% of the images. To minimize confusion with A, we further required (2) that the magnitude of A fall within 4 times the median absolute deviation (MAD) of its average magnitude in each band. Failure to meet this criterion eliminated an additional $\approx 5\%$ of data in J and $\approx 7\%$ in K_S . Lastly, (3) data were only accepted if the scatter of the reference star calibrations for a given image was less than 4σ above the average for each band. In the end, approximately 85% of the J - and K -band images (187 out of 223 for J and 362 out of 422 for K_S) and all 17 H -band images were selected.

The J and K_S light curves are shown in Figure 3 phased on the ephemeris derived below. The ellipsoidal modulation is evident in the light curves and shows up quite clearly in the J -band light curves from 2008.

¹http://www.ipac.caltech.edu/2mass/releases/allsky/doc/sec4_8.html

The agreement between the light curves from 2006/2007 and the light curves from 2008 is generally good, although the incomplete phase coverage hinders this comparison. The light curves disagree somewhat near orbital phase 0.0, which corresponds to the inferior conjunction of the companion star. The light curves near this phase appear to be “filled in” during the 2006-2007 period. Apart from the difference near phase zero, there does not seem to be any significant change in the mean brightness level from one year to the next. The modest differences that do exist are likely attributable to changes in the disk. A similar but much greater degree of disk variability in quiescence has been seen in the black hole candidate A0620-00 (Cantrell et al. 2010).

2.2. Spectroscopy

We obtained moderate resolution spectra of J1550 using the Magellan Echellette Spectrograph (MagE; Marshall et al. 2008) and the Clay telescope at LCO on the nights of 2008 May 6, June 28, and August 3-4. For the May observations the slit and resolving power were respectively $1''.0$ and $R = 4200$; for all other observations the slit was $0''.85$ and $R = 4950$. The skies were clear and the seeing was usually $\leq 0''.8$. The exposure times were typically 1200 seconds each, and ThAr lamp exposures were obtained frequently throughout the observing runs. The images were reduced with tasks in the IRAF ‘ccdproc’ and ‘echelle’ packages. After the bias was subtracted from each image, pairs of images were combined using a clipping algorithm to remove cosmic rays. This process yielded three spectra from May, three spectra from June, and 13 spectra from August. The resulting images were flat-fielded using a normalized master flat and then rotated in order to align the background night sky emission lines along the columns. After the background emission lines were rectified, the spectra from individual orders were optimally extracted. The signal-to-noise ratio of the extracted spectra were typically between 5 and 10 per pixel in the best echelle order.

3. Analysis and Results

3.1. Radial Velocities of the Secondary Star

For the MagE spectra of J1550 there is a single echelle order that covers the region between the interstellar sodium D lines and $H\alpha$ that we used to determine radial velocities. The bluer orders deliver poor signal-to-noise because the source is quite red, and the redder orders are unusable because of heavy fringing and strong telluric features. The ‘fxcor’ routine in IRAF (based on the cross-correlation technique given in Tonry & Davis 1979) was used to measure the radial velocities. We used a spectrum of the K3III star HD 181110 as the template. The same template star was used by Orosz et al. (2002) for the analysis of their 8.2m VLT spectra. The three MagE spectra from May gave good cross-correlation peaks, as did nine of the spectra from June and August. The values of the Tonry & Davis ‘ r ’ parameter were generally between 3 and 5 for these spectra. In the analysis below we used only the 12 spectra from which usable radial velocity measurements were derived.

It proved to be difficult to combine the radial velocities obtained by the VLT (17 observations) and by Magellan (12 observations). The velocities from each data set were fitted to a sine curve of the form $V(\phi) = K \sin(\phi) + \gamma$, where ϕ is the orbital phase. Even though the same template star was used for both analyses, the γ -velocities differed by 70 km s^{-1} . By using common stars that were observed by both telescopes, it was discovered that the zero-point of the VLT velocities is uncertain by at least 30 km s^{-1} . In addition, it is possible that the template star is a single-lined binary star with a moderately long

period, resulting in a small change in its radial velocity between the two runs. To combine the two data sets, we simply removed the fitted γ -velocity appropriate for each set from each individual radial velocity. For the combined set containing 29 radial velocities, a sine curve was fitted yielding an orbital period of $P = 1.5420435 \pm 0.0000069$ days and a radial velocity semiamplitude of $K_2 = 365.5 \pm 7.1$ km s⁻¹. The radial velocities and the best-fitting sine curve are shown in Figure 4. In our earlier work (Orosz et al. 2002), the VLT spectra alone yielded $K_2 = 349 \pm 12$ km s⁻¹, and fitting both the light-curve and velocity data gave $352.2 \leq K_2 \leq 370.1$ km s⁻¹ (1σ). Although the VLT observations were obtained shortly after a weak minioutburst, the source appeared to be very near X-ray quiescence (Orosz et al. 2002). This impression seems to be confirmed when the Magellan and radial velocities are compared in Figure 4, where there appears to be no systematic differences between the Magellan and VLT radial velocities.

3.2. The Rotational Velocity of the Secondary Star and the Disk Fraction

In order to measure the projected rotational velocity of the secondary star and the fraction of light contributed by the accretion disk (the “disk fraction”), we made a “restframe” spectrum from the nine spectra obtained in June and August (i.e. spectra that show cross-correlation peaks and were also obtained with the 0.85 slit). Each spectrum (from the single echelle order) was normalized to its continuum using a polynomial fit and Doppler shifted to zero velocity. The resulting nine normalized spectra were then averaged with no clipping or rejection of bad pixels. The “broadening function” technique developed by Rucinski (2002) was used to measure the projected rotational velocity of the secondary. The spectrum of the K3III star was used as the high signal-to-noise sharp-lined reference spectrum. The broadening kernel² (hereafter the Broadening Function or BF) appropriate for the restframe spectrum was derived, and is shown in Figure 5. The BF from the rest frame spectrum is well-fitted by a Gaussian with a FWHM of 65.4 ± 2.5 km s⁻¹.

We then performed a few simple numerical experiments in order to map the relationship between the BF FWHM and the rotational velocity of the star. A spectrum of the K4 III star HD 181480 (observed using MagE and the 0.85 slit) was normalized to its continuum and rotationally broadened by various rotational velocities using the familiar analytic broadening kernel (e.g. Gray 1992) with a limb darkening coefficient of $\epsilon = 0.6$. The BFs of the rotationally broadened spectra were derived using the same template that was used for the J1550 restframe spectrum. The plot of the input rotational velocity vs. the Gaussian FWHM of the derived BFs is shown in Figure 6. For large rotational velocities, the Gaussian FWHM roughly gives the input rotational velocity, as expected. Not surprisingly, the curve begins to flatten out at low velocities where the input rotational velocity is comparable to the spectral resolution. The observed Gaussian FWHM for J1550 of 65.4 ± 2.5 km s⁻¹ seems to imply a rather low rotational velocity of around 50 km s⁻¹. In our previous work (Orosz et al. 2002), a provisional value of about 90 km s⁻¹ was derived from spectra of lower resolution (3.6 Å FWHM). The MagE results clearly do not support this. The width of the BFs from the individual spectra are narrow (to the extent that one can measure them). One expects that the process of making a restframe spectrum would result in a BF that is as wide or wider than the individual BFs. Thus it seems very unlikely that the narrow BF width is an artifact of the process that was used to make the restframe spectrum. Since the actual rotational velocity of the companion star presumably has not changed, it appears that the value of 90 km s⁻¹ derived from the VLT was spurious and due to the low resolving

²Basically, the broadening kernel is the function needed to convert a hypothetical spectrum of a non-rotating star into its observed restframe spectrum.

power of the averaged spectrum.

Next, we used the technique outlined in Marsh, Robinson, & Wood (1994) to decompose the restframe spectrum into its stellar and disk components. This was the same technique we used in our previous paper (Orosz et al. 2002). Briefly, a template spectrum is normalized to its continuum, and the Doppler shift between it and the J1550 restframe spectrum is removed. The template spectrum is scaled by a weight w and subtracted from the J1550 restframe spectrum. A polynomial is fit to the residuals and the rms of the fit is recorded. The value of w that gives the lowest rms is taken to be the optimal weight for that template. The four template stars that gave the best decompositions for the VLT spectra (Orosz et al. 2002) were re-observed with MagE and the $0''.85$ slit. The spectral types of the templates are G8IV, K1III, K3III, and K4III. The K3III template gave the lowest rms using $w = 0.61$, and the G8IV template gave the worse rms values. Based on this, we adopt a spectral type of K3III, with an uncertainty of perhaps 1 subclass.

The K3III spectrum was then rotationally broadened by various amounts between 40 and 90 km s⁻¹, and the decomposition process was repeated. For each input value of $V_{\text{rot}} \sin i$ the minimum rms was recorded. Figure 7 shows the rms vs. the input rotational velocity. The rms is at its minimum value at an input rotational velocity of $V_{\text{rot}} \sin i = 57$ km s⁻¹. As was the case with the BF analysis, a rotational velocity as high as 90 km s⁻¹ is clearly ruled out.

Based on the BF analysis and on the results shown in Figure 7, we adopt a 1σ range of the projected rotational velocity of $50 \leq V_{\text{rot}} \sin i \leq 60$ km s⁻¹. Assuming the secondary star is rotating synchronously with its orbit and that it fills its Roche lobe, there is a relatively straightforward relation between the observed (projected) rotational velocity of the star, its K -velocity, and the mass ratio of the binary (e.g. Wade & Horne 1988). We show from the dynamical modeling discussed below that the projected rotational velocity of the star cannot be much below 50 km s⁻¹, assuming a reasonable mass for the star. Our adopted values of $V_{\text{rot}} \sin i = 55 \pm 5$ km s⁻¹ and $K_2 = 365.5 \pm 7.1$ km s⁻¹ imply a rather extreme mass ratio of $Q \equiv M/M_2 \approx 30$.

Figure 8 shows the rms vs. w for the K3III template, rotationally broadened using $V_{\text{rot}} \sin i = 57$ km s⁻¹. The minimum of the curve is well-defined, and gives a *disk* fraction of 0.39, where the disk fraction is taken to be $1 - w$. The BF of the smoothest residual spectrum from the decomposition was computed and is shown in Figure 5. There is no significant peak in the BF, which is a good indication that the stellar absorption lines have been removed.

We adopt a disk fraction of 0.39 ± 0.05 , at an effective wavelength of 6200 Å, which we take to be the R -band in the ellipsoidal modeling discussed below. For comparison, Orosz et al. (2002) adopted a V -band disk fraction of $k_V = 0.30 \pm 0.05$. We believe the R -band value of $k_R = 0.39 \pm 0.05$ is more reliable than the V -band determination of $k_V = 0.30 \pm 0.05$ owing to the better resolution of the MagE spectra.

3.3. Temperature of the Secondary Star and Extinction

The spectral type of the star can be used to estimate its temperature. However, the temperature corresponding to a given spectral type depends on the luminosity class, with main-sequence stars having higher temperatures than the corresponding giants. For example, Straižys & Kuriliene (1981) give $T_{\text{eff}} \approx 4700$ K for a K3V star, and $T_{\text{eff}} \approx 4250$ K for a K3III star. A variation of ± 1 spectral subtype implies a temperature in the range $T_{\text{eff}} \gtrsim 4100$ K (the K4III star) and $T_{\text{eff}} \lesssim 4850$ K (the K2V star). However, the surface gravity of the secondary star in J1550 is larger than the nominal surface gravity of a “normal” K3III

star. Straizys & Kuriliene (1981) give $\log g \approx 2.38$ for a K3III star. The surface gravity of the star in J1550 is well determined from the dynamical model discussed below and is $\log g = 3.43$. For the nominal main sequence K3V star Straizys & Kuriliene (1981) give $\log g \approx 4.56$. If we do a simple interpolation in $\log g$, the tables of Straizys & Kuriliene (1981) would give $T_{\text{eff}} \approx 4475$ K for a K3 star with a surface gravity matching the J1550 secondary.

The NIR is especially useful for determining the intrinsic color of the star and the reddening to the source because it only very weakly depends on the assumed reddening law (see Draine 2003). Thus, using NIR data one can place simultaneous constraints upon the extinction to the source and the spectral type of the star. Vuong et al. (2003) has directly measured the relationship between X-ray absorption and NIR extinction using several young stellar objects embedded in the nearby molecular cloud ρ Ophiuchi. For each source, they measure N_H from X-ray edge absorption and determine J -band extinction A_J . They find

$$A_J(\text{mag}) = \frac{N_H}{(5.6 \pm 0.4) \times 10^{21} \text{cm}^{-2}}, \quad (2)$$

which is significantly below the optically determined Galactic relationship (e.g. rescaling the fit of Predehl, P.; Schmitt (1995) to NIR bands gives $N_H/A_J = 6.75 \times 10^{21} \text{cm}^{-2} \text{mag}^{-1}$). Vuong and collaborators find that this apparent discrepancy is completely explainable by nonstandard abundances present in the local ISM (using values taken from Wilms et al. 2000).

Since the NIR reddening law depends only modestly on the reddening parameter R_V , NIR colors are relatively insensitive to the line-of-sight dust properties. We obtain model extinction estimates using the full NIR extinction curves modeled by the “fmcure” routines of Fitzpatrick (1999) and the filter properties of PANIC (Martini et al. 2004). We assume average Galactic reddening $R_V = 3.1$ (Cardelli, Clayton, & Mathis 1989) to convert between A_V and $A_{J,H,K}$ and note that the differences introduced into A_J/A_K by the full range of R_V is a negligible source of error.

We used a Monte Carlo approach to determine extinction, while incorporating all relevant uncertainties. Adopting $N_H = (8.0 \pm 0.4) \times 10^{21} \text{cm}^{-2}$ (90% confidence), as measured by Miller et al. (2003), and assuming a Gaussian systematic uncertainty on N_H/A_J of $\sigma_{\text{sys}} = 0.6 \times 10^{21} \text{cm}^{-2} \text{mag}^{-1}$ (i.e., one-half the difference arising from using local vs. standard Galactic ISM abundances), we obtained $A_J = 1.17 \pm 0.11$, $A_H = 0.762 \pm 0.074$, and $A_K = 0.507 \pm 0.050$.

The observed NIR color of the secondary star is $J - K_S = 1.27 \pm 0.04$. The unreddened color would then be $(J - K_S)_0 = 0.610 \pm 0.083$ using $A_K = 0.507 \pm 0.050$. We have used zero-point uncertainties of 0.02 mag for both J and K_S to find the uncertainty in $(J - K_S)_0$. In order to find the temperature of the secondary star from the observed $(J - K_S)_0$, we used synthetic photometry from the NEXTGEN models (Hauschildt, Allard, & Baron 1999a; Hauschildt et al. 1999b). Using these models, we can compute the $J - K_S$ color of the secondary star given its temperature and gravity. Owing to the nature of Roche geometry, the gravity is strongly constrained by the ellipsoidal models (discussed below) for a wide range of temperatures, and we adopt $\log g = 3.43$ for these calculations. We found from extensive experimentation with the synthetic ellipsoidal light curves discussed below that the addition of an accretion disk that satisfies the constraint of a disk fraction of 0.39 at 6200 Å does not significantly alter the $J - K_S$ color of the star, *despite the fact that the computed disk fractions in J and K are not zero*. The top of Figure 9 shows the value of $(J - K_S)_0$ as a function of temperature. The observed value of $(J - K_S)_0 = 0.610$ implies a temperature of about 4450 K, in good agreement with the temperature derived from the spectral type above. The 1σ range on the color maps into a temperature range of $4300 \lesssim T_{\text{eff}} \lesssim 4650$ K.

We did a Monte Carlo simulation to derive the distribution of allowed temperatures, given the observed

$J - K_S$ color of 1.27 ± 0.04 . We varied the model input temperature in steps of one degree between 3800 and 5900 K. At each input temperature, 40,000 synthetic reddened $J - K_S$ colors were constructed by drawing values of A_K and zero-point uncertainties from Gaussian distributions of the appropriate width. This process left us with about 84,000,000 $T_{\text{eff}}, J - K_S$ pairs. We then selected the pairs with a color between $1.265 \leq J - K_S \leq 1.275$ and computed a frequency distribution of the temperatures from that interval. The resulting histogram of temperatures is shown in the bottom of Figure 9. The distribution has two main peaks near 4450 and 5000K, with the most likely temperature near 4450 K. The interval of $4207 \leq T_{\text{eff}} \leq 5068$ K contains 68% of the probability with equal probabilities at each end. Thus based on the color alone, temperatures around 5100 K or so cannot be ruled out with high confidence.

As noted above, the spectral type of the star implies a temperature near 4475 K for a K3III spectral type and about 4700 for a K3V spectral type. These temperatures are near the leftmost peak in the histogram in Figure 9. For temperatures greater than about 5200 K, the spectral type would be G8 or earlier for luminosity class V, which can be ruled out based on the observed spectral type. For the purposes of the ellipsoidal modeling discussed next, we adopt a temperature range of $4200 \leq T_{\text{eff}} \leq 5200$ K, where the lower end is roughly the 1σ lower limit determined from Figure 9 and the upper end is imposed by the spectral type.

3.4. Simultaneous Fits to Light and Velocity Curves

We used the ELC code of Orosz & Hauschildt (2000) to derive a dynamical model of J1550. The reader is referred to Orosz et al. (2002) for a thorough description of the assumptions and techniques used. The data modeled include optical light curves (V , g' , r' , i' , and z' from Orosz et al. 2002), NIR light curves (J and K_s discussed here), and radial velocities from the VLT (Orosz et al. 2002) and Magellan. We have three extra constraints: the disk fraction, the rotational velocity of the star, and the fact that the X-ray source is not eclipsed. We used ELC’s genetic and Monte Carlo Markov Chain optimizers to arrive at the solutions. We have 10 free parameters in the model (the parameter ranges searched are given in parentheses): the inclination i (50.0–81.0 deg), the mass of the donor star M_2 (0.1–3.0 M_\odot), the K -velocity of the donor star K_2 (336–396 km s $^{-1}$), the effective temperature of the donor star T_2 (4200–5200 K), the orbital period P (1.5420–1.5421 days), the time of the inferior conjunction of the donor star [HJD 2,452,000 + (53.8–54.2)], and four parameters to specify the accretion disk, namely the radius scaled to the Roche lobe radius (0.60–1.0), the opening angle of the rim (0.5–12.0 deg), the temperature of the inner rim (1500–20000 K), and the exponent on the radial temperature profile (–0.9–0.0). We have found that the search of parameter space is more efficient if the mass of the donor star and its K -velocity are used to set the scale of the binary instead of using the mass ratio Q and the orbital separation a . We assume a circular orbit and synchronous rotation. We also assume that X-ray heating can be neglected in the quiescent state (discussed further below).

Because of differences between the J and K_S light curves between 2006/2007 and 2008 (Figure 3), and because we have two measurements of the disk fraction (the V -band measurement in Orosz et al. 2002 and the R -band measurement discussed here), we fit the data using eight combinations: optical light curves only, optical light curves and the 2006/2007 NIR light curves, optical light curves and the 2008 NIR light curves, and optical light curves plus all NIR light curves. For each of these four cases, we had two constraints on the disk fraction: $k_V = 0.30 \pm 0.05$ (Orosz et al. 2002) and $k_R = 0.39 \pm 0.05$ derived here. For the sake of the discussion we label these eight cases as models A, B, ... H (see Table 2). For each combination the genetic code was run three times from different starting locations, and the Markov code was run twice. For each case a total of 250,000 to nearly one million models were computed. When run for a sufficient

number of iterations, both the genetic code and the Markov chain are insensitive to the precise ranges for the parameters, provided the actual best-fitting parameters are within the specified ranges. The ranges used for the fitted parameters were chosen to be large enough so that they contained the model with the lowest χ^2 . Owing to the multiple runs of the optimizers and the large number of models computed, we are confident that the global minimum in χ^2 was reached in each case.

The results of the fitting are shown in Table 2. There are some features in the table that should be noted. First, the K -velocities found from each situation are slightly different (although well within their respective 1σ errors). This is because the computation of the radial velocity curve in ELC is not completely decoupled from the light curves (e.g. the model atmosphere intensities are tabulated in terms of the gravity $\log g$ which is given in physical units), and because ELC also computes corrections to the radial velocity curves caused by the distortion of the secondary star (Wilson & Sofia 1976; Eaton 2008). Second, the range in the inclination values is not terribly large. The lowest inclination is $57.7 \pm 4.3^\circ$ for model C (i.e. the combination of the 2006/2007 NIR light curves and the optical light curves with $k_V = 0.30 \pm 0.05$) and the largest inclination is $77.1 \pm 7.1^\circ$ for model B (the combination of the optical light curves with $k_R = 0.39 \pm 0.05$). Hence the range of derived black hole masses is relatively constrained: $(8.9 \pm 1.1 M_\odot) < M < (13.9 \pm 1.6 M_\odot)$. Third, since the same optical light curves are fitted in all 8 cases, the χ^2 values for the fits to the optical light curves give us a way to judge the relative goodness-of-fit of each situation. The situation that gives the best fits to the optical light curves is for model B (optical curves only and $k_R = 0.39 \pm 0.05$). When we consider the situations where NIR light curves are also fit, model F has the best fits to the optical light curves. Fitting the 2006/2007 NIR light curves with the optical light curves (models C and D) or the combined NIR light curves and the optical light curves (models G and H) results in significantly worse fits to the optical data. Thus it seems that the shapes of the optical light curves are more consistent with the shapes of the 2008 NIR light curves. Considering the cases where the 2008 NIR light curves are fit with the optical light curves (models E and F), the range in the inclination (and hence the black hole mass) are further constrained: $(66.4 \pm 6.9^\circ) < i < (74.7 \pm 3.8^\circ)$ and $(9.1 \pm 0.6 M_\odot) < M < (10.6 \pm 1.3 M_\odot)$.

As noted above, we believe our measurement of the R -band disk fraction of 0.39 ± 0.05 is more secure than the V -band disk fraction adopted by Orosz et al. (2002) owing to the higher resolution of the Magellan spectra. In most cases, using the R -band disk fraction as an extra constraint gives better fits to the optical data compared to when the V -band disk fraction constraint is used. Looking at cases when the R -band disk fraction constraint was used (models D, F, and H), and where NIR data was used, model F gives the best overall fit to the optical data. Thus, for the final values of the fitted and derived parameters, we adopt the results derived from model F. Figure 10 shows the phased light curves and the best-fitting models.

Finally, we note that we have assumed the light curves have symmetry in phase about $\phi = 0.5$, and that the overall level of light has stayed more or less constant from year to year. Both these assumptions may not be strictly true. Cantrell et al. (2008) have shown that A0620-00 has different optical “states” while in X-ray quiescence, ranging from the relatively quite “passive” state to the “active” state where the brightness level and activity levels are elevated relative to the passive state. In addition, Cantrell et al. (2010) have shown that even in the passive state the optical light and NIR curves of A0620-00 can change with time. These authors showed that a bright spot on the accretion disk can account for most of the observed changes. It is difficult to directly assess the importance of asymmetry or X-ray heating in the light curves, especially in the NIR. On the other hand, as noted above, the spread in the inclination angles for all models is not that large, so we do not expect the masses we report to have unreasonably large systematic errors.

3.5. Distance

We compute the distance to the source using the synthetic photometry code based on the NEXTGEN models. Given a stellar radius, gravity, and temperature, we compute the absolute magnitude of the star in the K_S filter. We adjust the absolute magnitude to account for the light from the accretion disk in the K_S band. Dereddening the apparent K_S magnitude, the distance then follows from the difference between the absolute and apparent magnitudes.

The distance and its uncertainty for each model in Table 2 was computed using a simple Monte Carlo code. For all models, we use an apparent magnitude of $K = 16.15 \pm 0.04$, where we have used a generous uncertainty to account for the zero-point error and the error in determining the mean magnitude from the ellipsoidal curve, an extinction of $A_K = 0.507 \pm 0.050$ (Section 3.3), and a stellar temperature drawn from the distribution shown in Figure 9. For individual models, the stellar radius, the gravity, and the computed K -band disk fraction and their uncertainties are listed in Table 2. Models A and B are fits to the optical data only, and as such do not have computed K -band disk fractions. For our adopted model F, the top panel of Figure 11 shows the derived probability distribution of the distance in kpc. The most likely distance is 4.38 kpc, with a 1σ range of $3.97 \leq d \leq 4.96$. For comparison Orosz et al. (2002) derived a distance of 3.9 ± 1.8 kpc for a secondary star mass of $0.5 M_\odot$. Our revised distance is much more precise because our dynamical model is more precise and because we are using K_S band observations where the extinction is minimal.

As an independent check, we computed the distance for the parameters from model F using the apparent J -band magnitude ($J = 17.42 \pm 0.04$) and extinction ($A_J = 1.17 \pm 0.11$). The bottom panel of Figure 11 shows the probability distribution for the distance in kpc. The most likely distance is 4.52 kpc, which is very close to the most likely distance derived using the K_S -band. However, owing to the larger uncertainty in the J -band extinction, the distance derived from J -band measurements has a larger uncertainty. The 1σ range for the J -band measurement is $3.87 \leq d \leq 5.36$ kpc, which is nearly as large as the 90% range on the K_S -band measurement.

Based on a reanalysis of the radio images obtained during the 1998 outburst, Hannikainen et al. (2009) constrained the source distance to be between 3.3 and 4.9 kpc based on absorption features seen in the radio spectrum. Our 1σ distance range is compatible with their range. Using $d = 4.4$ kpc, the apparent separation velocity between two ejection events observed in 1998 is $1.7c$, and the intrinsic velocity is $\gtrsim 0.9c$ (Hannikainen et al. 2009). Corbel et al. (2002) observed the radio jets in June of 2000 and again in January of 2002. They measured an average proper motion for the approaching jet of 32.9 ± 0.7 milliarcseconds (mas) day^{-1} and an average proper motion for the receding jet of 18.3 ± 0.7 mas day^{-1} . At a distance of 4.4 kpc, these proper motions correspond to large apparent velocities of $0.84c$ and $0.47c$. Corbel et al. (2002) also detected material from the approaching jet at X-ray wavelengths in 2000 and in 2002. The proper motions of the X-ray jet were 21.2 ± 7.2 mas day^{-1} between 2000 June and September, and 10.4 ± 0.9 mas day^{-1} between 2000 September 2002 and March. At a distance of 4.4 kpc, these proper motions correspond to apparent separation velocities of $0.55c$ and $0.27c$, respectively. Our best-fit values also imply that the remarkable X-ray flare of 1998 September 19-20 (see §1) reached a luminosity of $0.4L_{\text{Edd}}$, as determined from dead-time corrected spectral analyses of the *RXTE* pointed observation near MJD 51076.016.

4. Discussion

4.1. The Mass of the Black Hole and the Binary Mass Ratio

The adopted value for the mass of the black hole is $9.10 \pm 0.61 M_{\odot}$ (Table 2). For comparison, Orosz et al. (2002) derived a mass of $9.56 \pm 1.2 M_{\odot}$ without using a constraint on the (projected) rotational velocity of the star, and $10.63 \pm 0.95 M_{\odot}$ when using a tentative value of $V_{\text{rot}} \sin i = 90 \pm 10 \text{ km s}^{-1}$ as an extra constraint. Using the rotational velocity as an extra constraint restricts the range of allowed mass ratios, and $V_{\text{rot}} \sin i = 90 \text{ km s}^{-1}$ gives $Q \approx 9$. We have shown here that the tentative value of $V_{\text{rot}} \sin i = 90 \pm 10 \text{ km s}^{-1}$ suggested by Orosz et al. (2002) is ruled out by the moderate resolution Magellan spectra. We have measured a much lower and definite value of $V_{\text{rot}} \sin i = 55 \pm 5 \text{ km s}^{-1}$, which implies a much more extreme mass ratio. For our adopted model F, $Q = 30.1 \pm 5.7$. The mass ratio of J1550 is one of the most extreme measured for a black hole binary. Only XTE J1118+480 has a more extreme value, with $Q \approx 42$ (Calvelo et al. 2009).

Both XTE J1550-564 and XTE J1118-480 showed periodic modulations known as superhumps in their light curves as they approached quiescence (Jain et al. 2001a; Zurita et al. 2006). Superhumps are thought to be caused by the precession of a tidally distorted disk in a system with an extreme mass ratio (Whitehurst 1988; Whitehurst & King 1991), and as noted above, both systems have very large mass ratios. Zurita et al. (1996) observed a 0.02 mag modulation during the early decline towards quiescence, which they attributed to a superhump. They also noted slight distortions in quiescent light curves obtained on two different nights, and these distortions were attributed to a residual superhump modulation.

Could the quiescent light curves of XTE J1550-564 also have some kind of residual superhump modulation? While it is true that the quiescent light curves of XTE J1118+480 shown in Zurita et al. (2006) had night-to-night changes, these changes may in fact be due to other reasons. For example, Cantrell et al. (2010) showed that quiescent light curves of A0620-00 can systematically change from night to night owing to changes in the accretion disk (mainly the location of the hot spot). As we noted in Section 3.4 above, it is hard to completely rule out night-to-night variations in the quiescent XTE J1550-564 light curves, whatever their cause. Given that we have light curves from different seasons, we don't expect our dynamical model to have large systematic errors.

Our refined measurement of the black hole mass, orbital inclination and the distance to J1550 are important for the measurement of the black hole spin and for the interpretation of the observed high-frequency X-ray QPOs. A full discussion of the spin of this source as derived from detailed X-ray spectral modeling will appear in a subsequent paper (Steiner et al., in preparation). We will briefly discuss here the implications for the QPOs, which have been observed in J1550 at frequencies up to 284 Hz. For a Schwarzschild black hole, the frequency of the innermost stable circular orbit (ISCO) would be at $\nu = 2199/(M_{\text{BH}}/M_{\odot}) = 242 \text{ Hz}$ for $M_{\text{BH}} = 9.10 M_{\odot}$ (Shapiro & Teukolsky 1983). Strohmayer (2001) pointed out that one of the high-frequency QPOs for GRO J1655-40 seemed to imply substantial spin for the black hole, since its frequency would be higher than the dynamical frequency of the accretion disk at the ISCO for the case of zero spin. By analogy, we might expect this to occur as well for J1550, given that the high-frequency QPOs appear to be similar, while both systems are transient sources of relativistic jets (Hannikainen et al. 2009; Corbel et al. 2002; Hjellming & Rupen 1995). However, this is not the case for J1550, since our new mass determination allows a dynamical frequency at the ISCO (for the case of zero spin) which is faster than the 276 Hz QPO seen from this source (Remillard et al. 2002a). That is, $\nu = 279$ when $M = 7.88 M_{\odot}$, which is 2σ smaller than its nominal best value.

4.2. Evolutionary Status of the Secondary Star

The mass donor star in J1550 must be highly evolved owing to its relatively low mass of $M_2 = 0.30 \pm 0.07 M_\odot$ and large radius of $R_2 = 1.75 \pm 0.12 R_\odot$ (see Table 2). We show here that the star follows the relatively simple “stripped giant” evolution in a similar manner to the donor star in V404 Cyg (King 1993). In this picture, the properties of the star depend very strongly on the core mass M_c and not on its total mass M_2 . Webbink, Rappaport & Savonije (1983) show that the mass and radius of the star depend on M_c as

$$\ln(L_2/L_\odot) = 3.50 + 8.11 \ln(M_c/0.25) - 0.61[\ln(M_c/0.25)]^2 - 2.13[\ln(M_c/0.25)]^3 \quad (3)$$

$$\ln(R_2/R_\odot) = 2.53 + 5.10 \ln(M_c/0.25) - 0.05[\ln(M_c/0.25)]^2 - 1.71[\ln(M_c/0.25)]^2, \quad (4)$$

where M_c is in units of M_\odot and is in the range $0.17 \lesssim M_c \lesssim 0.45$. A core mass of $M_c = 0.1661$ is needed to get a radius of $1.75 R_\odot$, although we note that this core mass is just below the nominal range over which the fitting relations apply. The luminosity at this core mass is $0.946 L_\odot$, which is consistent with the value we derived ($1.05^{+0.60}_{-0.33} L_\odot$). Using Eqn. (33) of King (1988), the mass transfer rate is

$$-\dot{M}_2 \approx 5.4 \times 10^{-9} \left(\frac{M_c}{0.25} \right)^{7.11} (M_2/M_\odot) \approx 9 \times 10^{-11} M_\odot \text{yr}^{-1}. \quad (5)$$

Orosz et al. (2002) attempted to estimate the mass transfer rate from X-ray spectral models. They derived a total X-ray fluence in the 2-100 keV band of $\approx 1.1 \text{ ergs cm}^{-2}$ during 1998–2001. Since that time, J1550 has had minor outbursts in January of 2002 (Swank et al. 2002; Belloni et al. 2002) and March of 2003 (Dubath et al. 2003; Kuulkers et al. 2003; Arefiev et al. 2004; Sturmer & Shrader 2005). As RXTE All-Sky Monitor data show, these events were much weaker in the soft X-rays (2-12 keV) than the events between 1998 and 2001 (Remillard & McClintock 2006). For a distance of 4.4 kpc, the isotropic energy release during 1998–2001 was about 2.52×10^{45} ergs. If we assume a radiative efficiency of 10% and also assume that the mass lost from the secondary star is all captured by the black hole, then a recurrence time between the major outburst episodes of about 157 years would be needed for the mass transfer rate given in Equation 5. This recurrence time would increase if we considered the additional energy release in the 2002 and 2003 events. If the black hole has a significant spin, then the efficiency of accretion can be higher, which would lead to a smaller recurrence time, all other things being equal.

As the core evolves, it grows in mass. According to King (1988), the final core mass will be $M_c^f = M_2^f = (M_c^0)^{0.75} \approx 0.26 M_\odot$. For a present-day mass of $M_2 = 0.3 M_\odot$ and a core mass of $M_c = 0.1661$, J1550 can continue to accrete at its present rate (Equation 5) for another $\approx 4.4 \times 10^8$ years. After the mass transfer has stopped, the final orbital period of the binary will be about 44 days.

5. Summary

Using new moderate-resolution optical spectroscopy and near-infrared photometry obtained with the 6.5m Magellan Telescopes, we have derived a much improved dynamical model of the X-ray binary and microquasar J1550. By combining our new radial velocity measurements with the 17 measurements obtained 2001 May at the 8.2m VLT and with light curves, we found an orbital period of $P = 1.5420333 \pm 0.0000024$ days and a radial velocity semiamplitude of $K_2 = 363.14 \pm 5.97 \text{ km s}^{-1}$, which together imply an optical mass function of $f(M) = 7.65 \pm 0.38 M_\odot$. We find that the projected rotational velocity of the secondary star is much smaller than the tentative value found by Orosz et al. (2002). Our new value is $V_{\text{rot}} \sin i = 55 \pm 5 \text{ km}$

s_1 , which implies a very extreme mass ratio of $Q \equiv M/M_2 \approx 30$. We modeled simultaneously the optical and near-infrared light curves and the radial velocity curve to derive system parameters. We found component masses of $M_2 = 0.30 \pm 0.07 M_\odot$ and $M = 9.10 \pm 0.61 M_\odot$ for the secondary star and black hole respectively. The radius of the secondary star is $1.75 \pm 0.12 R_\odot$. Using this radius, the average K_S magnitude, and an extinction of $A_K = 0.507 \pm 0.050$ mag, a distance of $4.38^{+0.58}_{-0.41}$ kpc is derived.

We thank Danny Steeghs for the use of telescope time at LCO. JFS thanks Paul Martini for his gracious support with the PANIC pipeline. This publication makes use of data products from the Two Micron All Sky Survey, which is a joint project of the University of Massachusetts and the Infrared Processing and Analysis Center/California Institute of Technology, funded by the National Aeronautics and Space Administration and the National Science Foundation. The work of JAO was supported in part by the National Science Foundation grant AST-0808145. CBD gratefully acknowledges support from the National Science Foundation grant AST-0707627. The work of JEM was supported in part by NASA grant NNX08AJ55G. JFS was supported by Smithsonian Institution Endowment Funds. RR acknowledges support from NASA via the contract for the instrument team of *RXTE* at MIT.

REFERENCES

- Arefiev, V. A., Revnivtsev, M. G., Lutovinov, A. A., & Sunyaev, R. A. 2004, *Astr.Let.*, 30, 669
- Belloni, T., Colombo, A. P., Homan, J., Campana, S., & van der Klis, M. 2002, *A&A*, 390, 199
- Calvelo, D. E., Vrtilek, S. D., Steeghs, D., Torres, M. A. P., Neilsen, J., Filippenko, A. V., & González Hernández, J. I 2009, *MNRAS*, 399, 539
- Cantrell, A. G., Bailyn, C. D., McClintock, J. E., & Remillard, R. A. 2008, *ApJ*, 673, 727
- Cantrell, A. G., Bailyn, C. D., Orosz, J. A., McClintock, J. E., Remillard, R. A., Froning, C. S., Neilsen, J., Gelino, D. M., & Gou, L. 2010, *ApJ*, 710, 1127
- Cardelli, J. A., Clayton, G. C., & Mathis, J. S. 1989, *ApJ*, 345, 245
- Carpenter, J. M. 2001, *AJ*, 121, 2851
- Corbel, S., Fender, R. P., Tzioumis, A. K., Tomsick, J. A., Orosz, J. A., Miller, J. M., Wijnands, R., & Kaaret, P. 2002, *Science*, 298, 196
- Corbel, S., Tomsick, J. A., & Kaaret, P. 2006, *ApJ*, 636, 971
- Draine, B. T. 2003, *ARA&A*, 41, 241
- Dubath, P., Revnivtsev, M., Goldoni, P., von Kienlin, A., Lund, N., Grebenev, S., & Kuulkers, E. 2003, *IAU Circ.* 8100
- Eaton, J. 2008, *ApJ*, 681, 562
- Fitzpatrick, E. L. 1999, *PASP*, 111, 63
- Gray, D. F. 1992, *The Observation and Analysis of Stellar Photospheres* (Cambridge: Cambridge Univ. Press)

- Hannikainen, D. C., Hunstead, R. W., Wu, K., McIntyre, V., Lovell, J. E. J., Campbell-Wilson, D., McColough, M. L., Reynolds, J., & Tzioumis, A. K. 2009, *MNRAS*, 397, 569
- Hauschildt, P. H., Allard, F., & Baron, E. 1999a, *ApJ*, 512, 377
- Hauschildt, P. H., Allard, F., Ferguson, J., Baron, E., & Alexander, D. R. 1999b, *ApJ*, 525, 871
- Hjellming, R. M., & Rupen, M. P. 1995, *Nature*, 375, 464
- Homan, J., Wijnands, R., van der Klis, M., Belloni, T., van Paradijs, J., Klein-Wolt, M., Fender, R., & Méndez, M. 2001, *ApJS*, 132, 377
- Honeycutt, R. K. 1992, *PASP*, 104, 435
- Jain, R. K., Bailyn, C. D., Orosz, J. A., McClintock, J. E., Sobczak, G. J., & Remillard, R. A. 2001a, *ApJ*, 546, 1086
- Jain, R. K., Bailyn, C. D., Orosz, J. A., McClintock, J. E., & Remillard, R. A. 2001b, *ApJ*, 554, L181
- Jain, R. K., Bailyn, C. D., Orosz, J. A., Remillard, R. A., & McClintock, J. E. 1999, *ApJ*, 517, L131
- King, A. R. 1988, *QJRAS*, 29, 1
- King, A. R. 1993, *MNRAS*, 260, L5
- Kuulkers, E. Remillard, R. A., & Miller, J. M. 2003, *ATel* 134
- Marsh, T. R., Robinson, E. L., & Wood, J. H. 1994, *MNRAS*, 266, 137
- Marshall, J. L., Burles, S., Thompson, I. B., Shetman, S. A., Bigelow, B. C., Burley, G., Birk, C., Estrada, J., Jones, P., Smith, M., Kowal, V., Castillo, J., Storts, R., & Ortiz, G. 2008, *SPIE*, 7014, 70145
- Martini, P., Persson, S.E., Murphy, D.C., Birk, C., Shetman, S.A., Gunnels, S.M., and Koch, E. 2004, *Proc. SPIE*, 5492, 1653
- Miller, J. M., Wijnands, R., Homan, J., Belloni, T., Pooley, D., Corbel, S., Kouveliotou, C., van der Klis, M., & Lewin, W. H. G. 2001, *ApJ*, 563, 928
- Miller, J. M., Marshall, H. L., Wijnands, R., Di Matteo, T., Fox, D. W., Kommers, J., Pooley, D., Belloni, T., Casares, J., Charles, P. A., Fabian, A. C., van der Klis, M., & Lewin, W. H. G. 2003, *MNRAS*, 338, 7
- Orosz, J., Bailyn, C., & Jain, R. 1998, *IAU Circ.* 7009
- Orosz, J. A., & Hauschildt, P. H. 2000, *A&A*, 364, 265
- Orosz, J. A., Groot, P. J., van der Klis, M., McClintock, J. E., Garcia, M. R., Zhao, P., Jain, R. K., Bailyn, C. D., & Remillard, R. A. 2002, *ApJ*, 568, 845
- Predehl, P., & Schmitt, J. H. M. M. 1995, *A&A*, 293, 889
- Remillard, R. A., Munro, M. P., McClintock, J. E., & Orosz, J. A. 2002a, *ApJ*, 580, 1030
- Remillard, R. A., Sobczak, G. J., Munro, M. P., & McClintock, J. E. 2002b, *ApJ*, 564, 962

- Remillard, R. A., & McClintock, J. E. 2006, *ARA&A*, 44, 49
- Rodríguez, J., Corbel, S., & Tomsick, J. A. 2003, *ApJ*, 595, 1032
- Rucinski, S. 2002, *AJ*, 124, 1746
- Shapiro, S. L., & Teukolsky, S. A. 1983, *Black holes, white dwarfs, and neutron stars: The physics of compact objects*, (Wiley-Interscience, New York)
- Smith, D. A., & *RXTE/ASM* teams 1998, *IAU Circ.* 7008
- Sobczak, G. J., McClintock, J. E., Remillard, R. A., Cui, W., Levine, A. M., Morgan, E. H., Orosz, J. A., & Bailyn, C. D. 2000, *ApJ*, 544, 993
- Skrutskie, M. F., Cutri, R. M., Stiening, R., Weinberg, M. D., Schneider, S., Carpenter, J. M., Beichman, C., Capps, R., Chester, T., Elias, J., Huchra, J., Liebert, J., Lonsdale, C., Monet, D. G, Price, S., Seitzer, P., Jarrett, T., Kirkpatrick, J. D., Gizis, J., Howard, E., Evans, T., Fowler, J., Fullmer, L., Hurt, R., Light, R., Kopan, E. L., Marsh, K. A., McCallon, H. L., Tam, R., Van Dyk, S., & Wheelock, S. 2006, *AJ*, 131, 1163
- Stetson, P. B., 1987, *PASP*, 99, 191
- Straizys, V. & Kuriliene, G. 1981, *Ap&SS*, 80, 353
- Strohmayer, T. E. 2001, *ApJ*, 552, L49
- Sturner, S. J., & Shrader, C. R. 2005, *ApJ*, 625, 923
- Swank, Smith, J. E., & Markwardt, C. 2002, *IAU Circ.* 7792
- Tonry, J., & Davis, M. 1979, *AJ*, 84, 1511
- Vuong, M. H., Montmerle, T., Grosso, N., Feigelson, E. D., Verstraete, L., & Ozawa, H. 2003, *A&A*, 408, 581
- Wade, R. A., & Horne, K. 1988, *ApJ*, 324, 411
- Webbink, R. F., Rappaport, S., & Savonije, G. J. 1983, *ApJ*, 270, 678
- Whitehurst, R. 1988, *MNRAS*, 232, 35
- Whitehurst, R., & King, A. 1991, *MNRAS*, 249, 25
- Wilson, R. E., & Sofia, S. 1976, *ApJ*, 203, 182
- Wilms, J., Allen, A., & McCray, R. 2000, *ApJ*, 542, 914
- Zurita, C., Torres, M. A. P., Steeghs, D., Rodríguez-Gil, P., Muñoz-Darias, T., Casares, J., Shahbaz, T., Martínez-Pais, I. G., Zhao, P., Garcia, M. R., Piccioni, A., Bartolini, C., Guarnieri, A., Bloom, J. S., Blake, C. H., Falco, E. E., Szentgyorgyi, A., & Skrutskie, M. 2006, *ApJ*, 644, 432

Table 1. Summary of Observations

UT Date	Telescope	Instrument	Filter or Resolution	Note
2001 May 24-27	VLT Antu 8.2m	FORS1	V	Orosz et al. 2002
2001 May 24-27	VLT Antu 8.2m	FORS1	3.6 \AA FWHM	Orosz et al. 2002
2001 June 1	ESO NTT 3.5m	SuSI2	V, R	Orosz et al. 2002
2001 June 26-28	Magellan Baade 6.5m	MagIC	r', i', z'	Orosz et al. 2002
2006 May 6	Magellan Baade 6.5m	PANIC	K_s	
2007 May 23-25	Magellan Baade 6.5m	PANIC	J, H, K_s	
2007 June 2-4, 21	Magellan Baade 6.5m	PANIC	J, K_s	
2008 April 14-16	Magellan Baade 6.5m	PANIC	J, H, K_s	
2008 May 6	Magellan Clay 6.5m	MagE	1.41 \AA FWHM	
2008 June 28	Magellan Clay 6.5m	MagE	1.21 \AA FWHM	
2008 August 3-4	Magellan Clay 6.5m	MagE	1.21 \AA FWHM	
2009 July 15	Magellan Baade 6.5m	PANIC	K_s	

Table 2. J1550 Adopted Parameters

parameter model designation	optical only		2006/7		2008		combined		adopted value
	$k_V = 0.30$ A	$k_R = 0.39$ B	$k_V = 0.30$ C	$k_R = 0.39$ D	$k_V = 0.30$ E	$k_R = 0.39$ F	$k_V = 0.30$ G	$k_R = 0.39$ H	
P (days)	1.5420341	1.5420341	1.5420396	1.5420394	1.5420335	1.5420333	1.5420366	1.5420369	1.5420333
T_0 (HJD 2,450,000+) ^a	± 0.0000036	± 0.0000031	± 0.0000031	± 0.0000055	± 0.0000037	± 0.0000024	± 0.0000027	± 0.0000051	± 0.0000024
	2053.9334	2053.9333	2053.9313	2053.9318	2053.9301	2053.9306	2053.9301	2053.9297	2053.9306
	± 0.0036	± 0.0038	± 0.0061	± 0.0041	± 0.0037	± 0.0039	± 0.0030	± 0.0045	± 0.0039
K_2 (km s ⁻¹)	364.55 ± 7.23	364.33 ± 6.20	366.55 ± 8.62	368.18 ± 8.08	362.90 ± 6.22	363.14 ± 5.97	364.91 ± 6.85	365.35 ± 6.07	363.14 ± 5.97
i (deg)	63.39 ± 4.76	77.09 ± 7.06	57.72 ± 4.30	65.50 ± 4.75	66.37 ± 6.90	74.69 ± 3.79	66.25 ± 3.99	70.97 ± 3.73	74.69 ± 3.79
M_2 (M_\odot)	0.39 ± 0.09	0.30 ± 0.08	0.48 ± 0.11	0.36 ± 0.12	0.37 ± 0.08	0.30 ± 0.07	0.41 ± 0.05	0.31 ± 0.10	0.30 ± 0.07
R_2 (R_\odot)	1.90 ± 0.13	1.74 ± 0.17	2.04 ± 0.16	1.85 ± 0.18	1.87 ± 0.12	1.75 ± 0.12	1.92 ± 0.12	1.76 ± 0.17	1.75 ± 0.12
$\log g$ (cgs)	3.471 ± 0.035	3.432 ± 0.049	3.501 ± 0.040	3.458 ± 0.045	3.465 ± 0.037	3.434 ± 0.033	3.478 ± 0.040	3.435 ± 0.046	3.434 ± 0.033
a (R_\odot)	12.84 ± 0.57	11.77 ± 0.46	13.67 ± 0.56	12.72 ± 0.53	12.49 ± 0.54	11.85 ± 0.28	12.60 ± 0.63	12.14 ± 0.31	11.85 ± 0.28
M (M_\odot)	11.57 ± 1.48	8.91 ± 1.10	13.94 ± 1.64	11.27 ± 1.47	10.64 ± 1.32	9.10 ± 0.61	10.89 ± 1.68	9.81 ± 0.74	9.10 ± 0.61
Q (M/M_2)	29.6 ± 6.6	29.8 ± 7.7	29.0 ± 8.0	31.5 ± 5.3	28.5 ± 6.9	30.1 ± 5.7	26.9 ± 4.6	32.0 ± 8.8	30.1 ± 5.7
luminosity (L_\odot)	$1.23^{+0.71}_{-0.39}$	$1.02^{+0.65}_{-0.34}$	$1.38^{+0.88}_{-0.41}$	$1.16^{+0.70}_{-0.39}$	$1.19^{+0.72}_{-0.36}$	$1.05^{+0.60}_{-0.33}$	$1.25^{+0.74}_{-0.38}$	$0.99^{+0.68}_{-0.30}$	$1.05^{+0.60}_{-0.33}$
disk fraction (J)	0.229 ± 0.051	0.338 ± 0.048	0.196 ± 0.052	0.267 ± 0.034	0.283 ± 0.045	0.348 ± 0.026	0.267 ± 0.034
disk fraction (K)	0.243 ± 0.058	0.336 ± 0.075	0.176 ± 0.086	0.236 ± 0.038	0.303 ± 0.054	0.362 ± 0.032	0.236 ± 0.038
computed distance (kpc)	$5.24^{+0.68}_{-0.55}$	$5.07^{+0.70}_{-0.63}$	$4.53^{+0.57}_{-0.41}$	$4.38^{+0.58}_{-0.41}$	$5.07^{+0.58}_{-0.41}$	$4.85^{+0.71}_{-0.55}$	$4.38^{+0.58}_{-0.41}$
χ^2 (optical) ^b	141.64	139.69	155.67	157.58	147.48	146.81	153.37	154.58	...
χ^2 (J) ^c	105.78	104.29	89.57	86.74	190.23	189.25	...
χ^2 (K) ^c	278.21	279.32	81.92	82.02	364.89	363.23	...
χ^2 (radial velocities)	26.04	26.19	28.32	28.29	25.98	25.92	25.48	25.32	...

Note. — The effective temperature of the secondary has been constrained to the range $4200 \leq T_{\text{eff}} \leq 5200$ K.

^aThe time of inferior conjunction of the secondary star.

^bThe sum of the χ^2 values for the V , g' , r' , i' , and z' light curves.

^cThe number of J -band data points is $N_J = 102, 85, 187$ for 2006/7, 2008, and combined, respectively. The number of K -band data points is $N_K = 278, 84, 362$ for 2006/7, 2008, and combined, respectively.

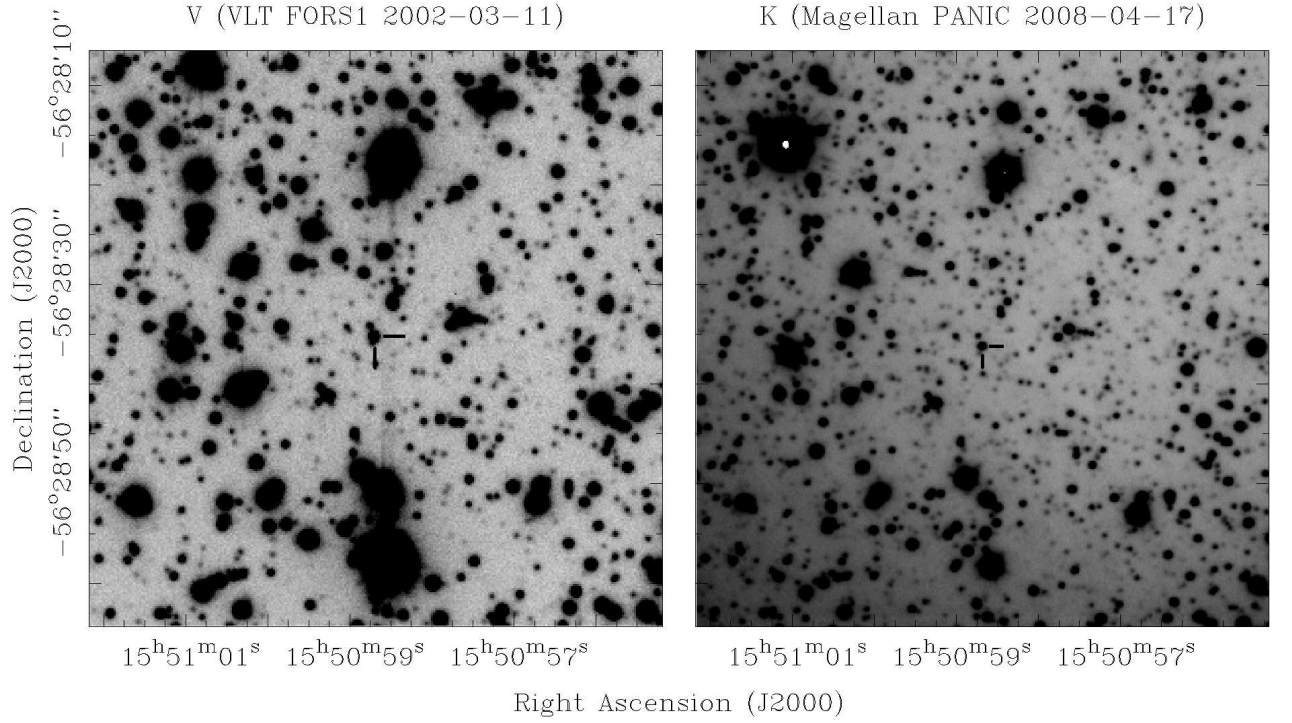


Fig. 1.— *V*-band (left) and *K*-band (right) finding charts of the field of J1550. Each image is approximately $1' \times 1'$. The *V* band image is a 300 second exposure obtained 2002 March 11 with the VLT/FORS1 instrument in $0''.6$ seeing. The composite *K*-band image was obtained with the Magellan/PANIC in seeing conditions typically $\leq 0''.6$. The net exposure time is 3000 seconds.

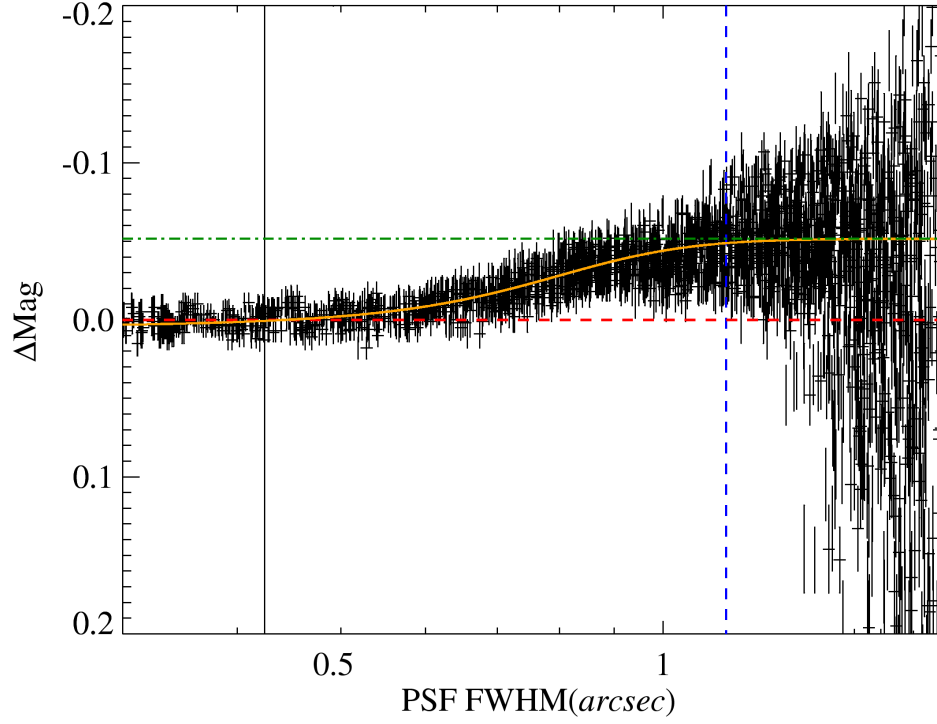


Fig. 2.— Simulated offsets in the J -band magnitude of J1550 vs. seeing derived from the Monte Carlo simulations. There is a prominent dependence of the derived magnitude on seeing, with an impact of up to 0.05 mag (denoted by the green dot-dashed line). The solid orange line, which is a fit to the trend, was used to correct the instrumental magnitudes of J1550 based on the seeing of the image. The vertical dashed blue line denotes the seeing cut adopted for the data, and the vertical black line denotes the best seeing during all of the runs.

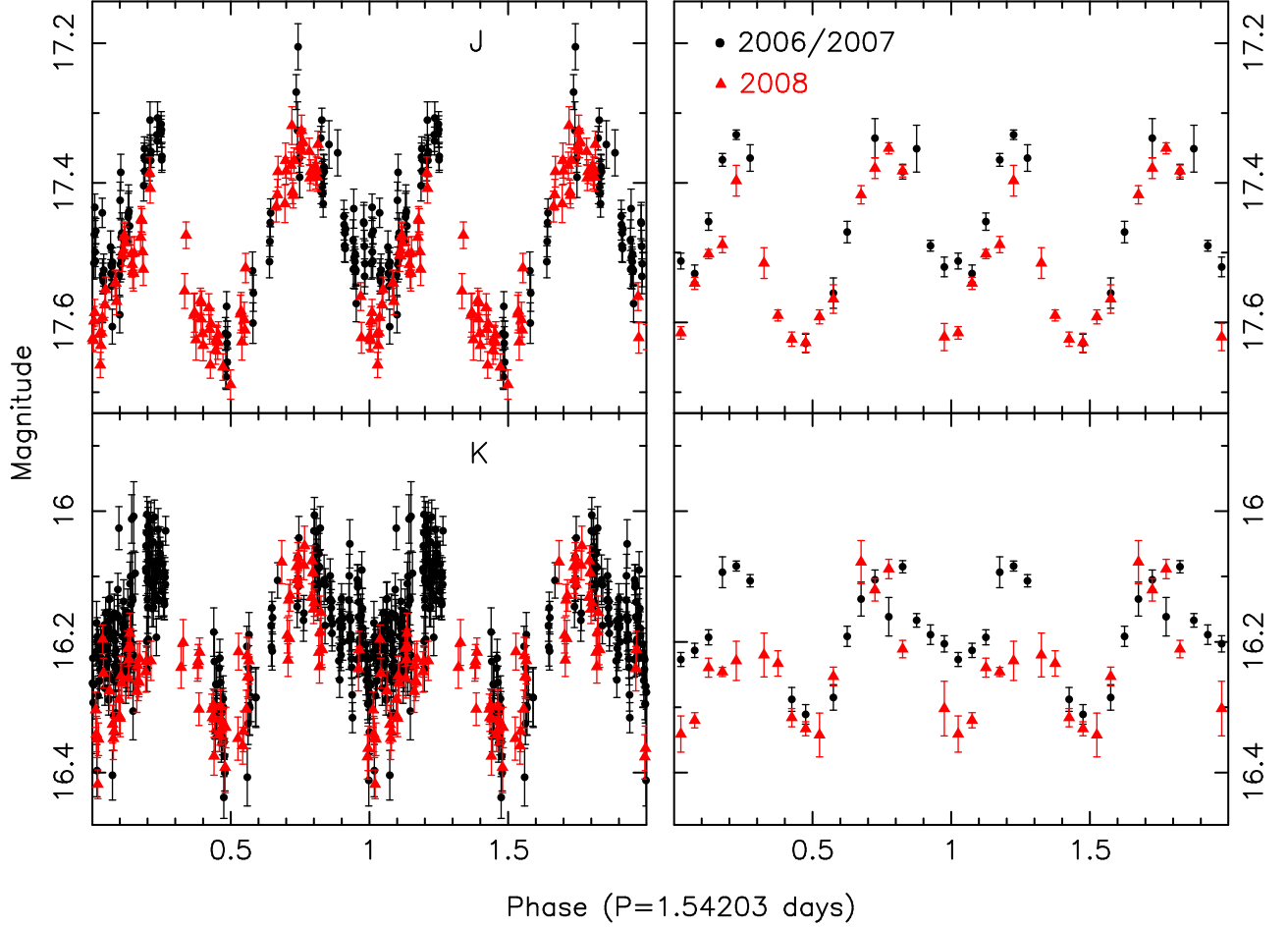


Fig. 3.— The phased J (top) and K_S (bottom) light curves of J1550, where phase zero corresponds to the time of the inferior conjunction of the secondary star. The panels on the left show the individual measurements, and the panels on the right show the binned light curves.

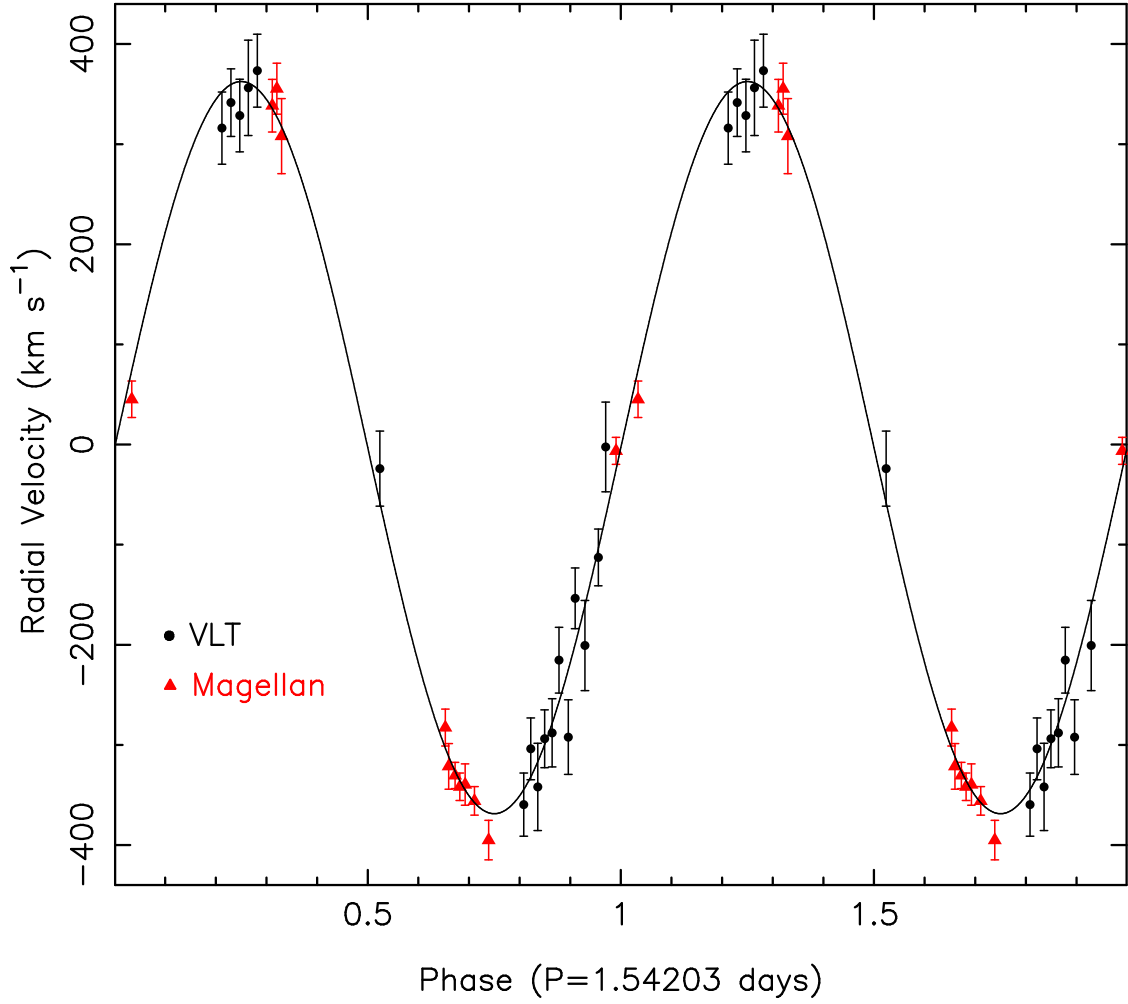


Fig. 4.— The phased velocity curve of J1550, where phase zero corresponds to the time of the inferior conjunction of the secondary star. The VLT radial velocities are shown with the filled circles and the MagE radial velocities are shown with the filled triangles. The solid line is the best-fit model assuming that the orbit is circular.

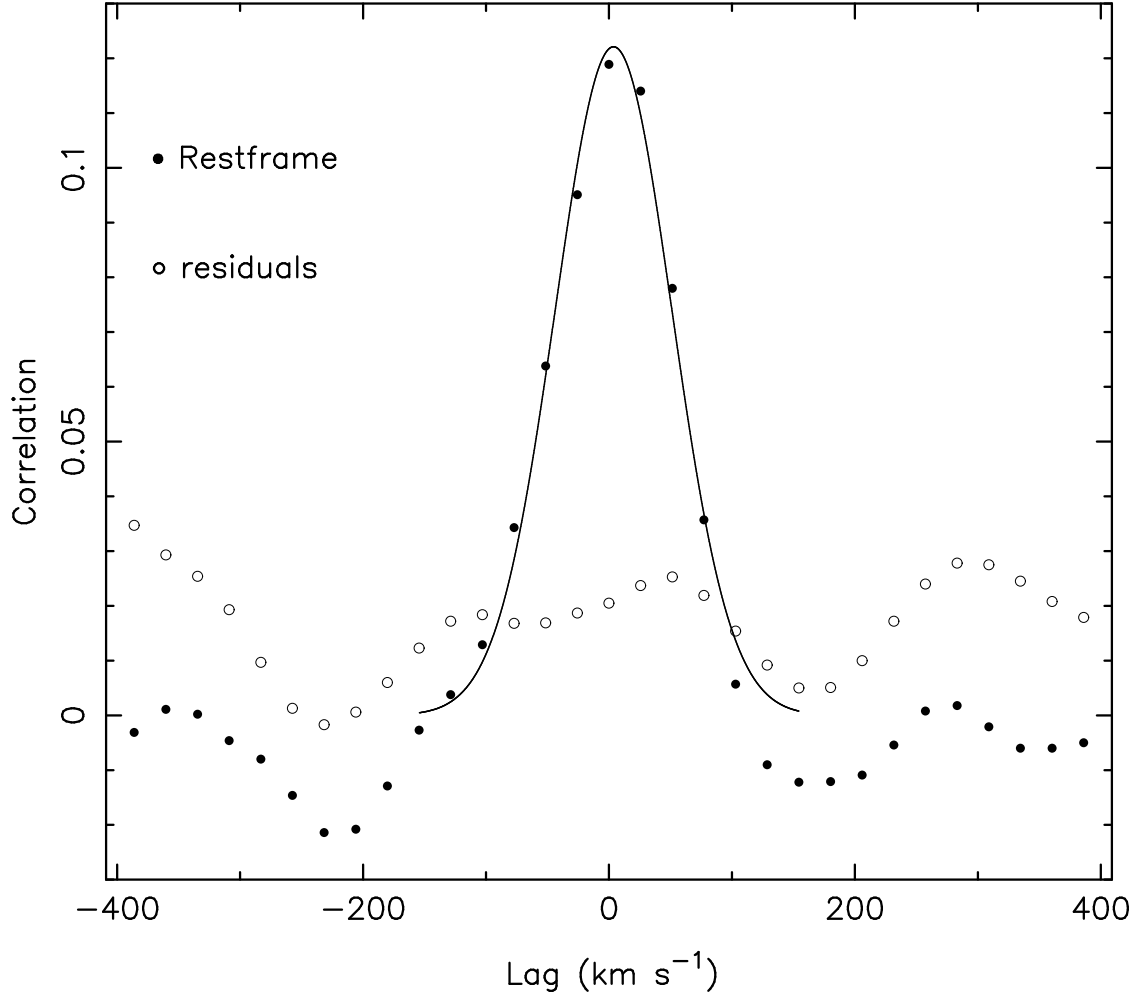


Fig. 5.— The broadening kernel derived from the J1550 restframe spectrum is shown by the filled circles. The best-fitting Gaussian (with a FWHM of 65.4 ± 2.5 km s⁻¹) is shown with a solid line. The broadening kernel derived from the residual spectrum (i.e. the difference between the restframe spectrum and the scaled spectrum of the template spectrum) is shown by the open circles. There is no discernible signal in the kernel of the residual spectrum, which is a good indication that the stellar absorption lines have been mostly removed.

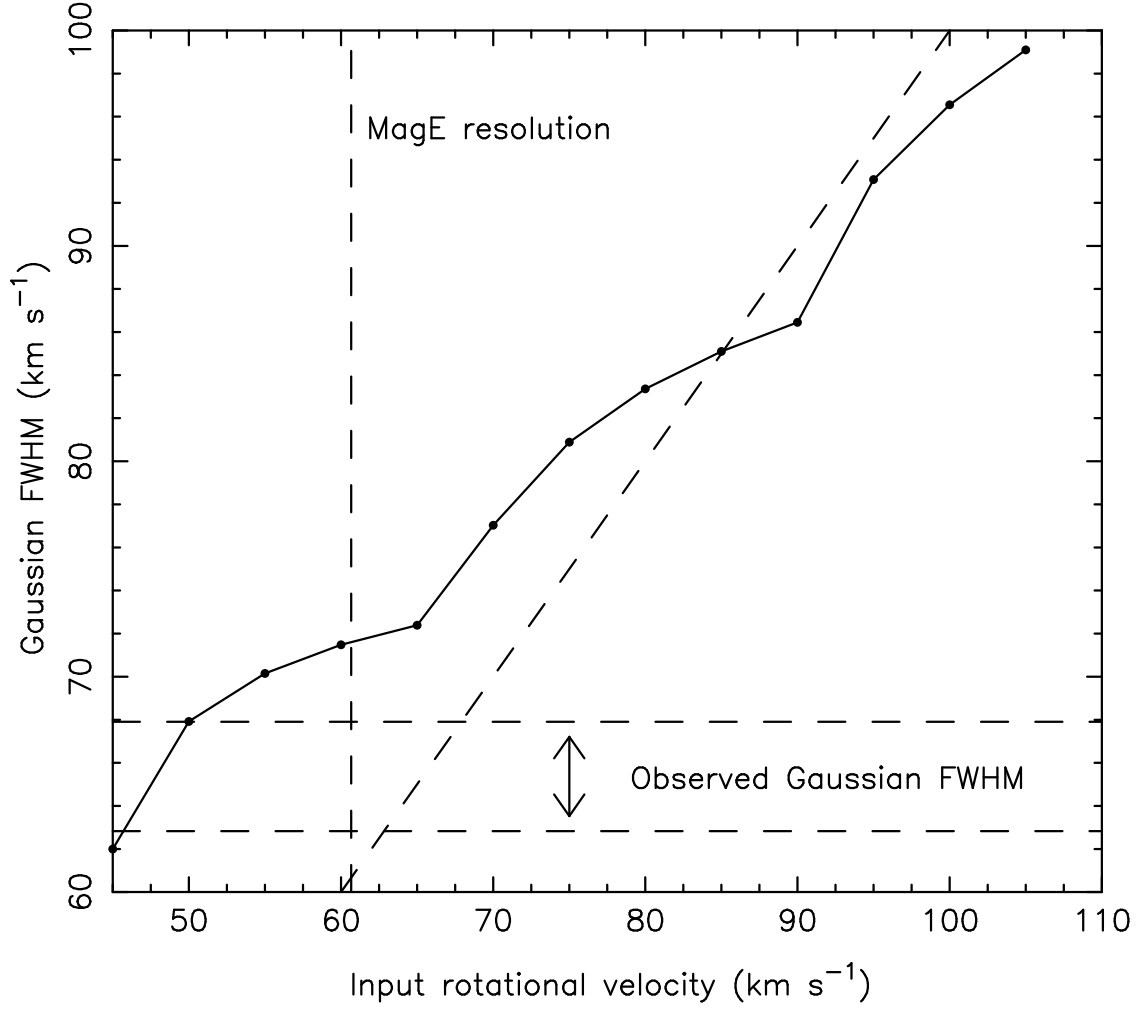


Fig. 6.— The Gaussian FWHMs of broadened reference star kernels are shown with filled circles. The diagonal dashed line indicates where the Gaussian FWHM equals the input rotational velocity. The vertical dashed line denotes the MagE spectral resolution, and the horizontal dashed lines denote the observed 1σ range of the Gaussian FWHM of the broadening kernel derived from the J1550 restframe spectrum (i.e. $\text{FWHM} = 65.4 \pm 2.5 \text{ km s}^{-1}$).

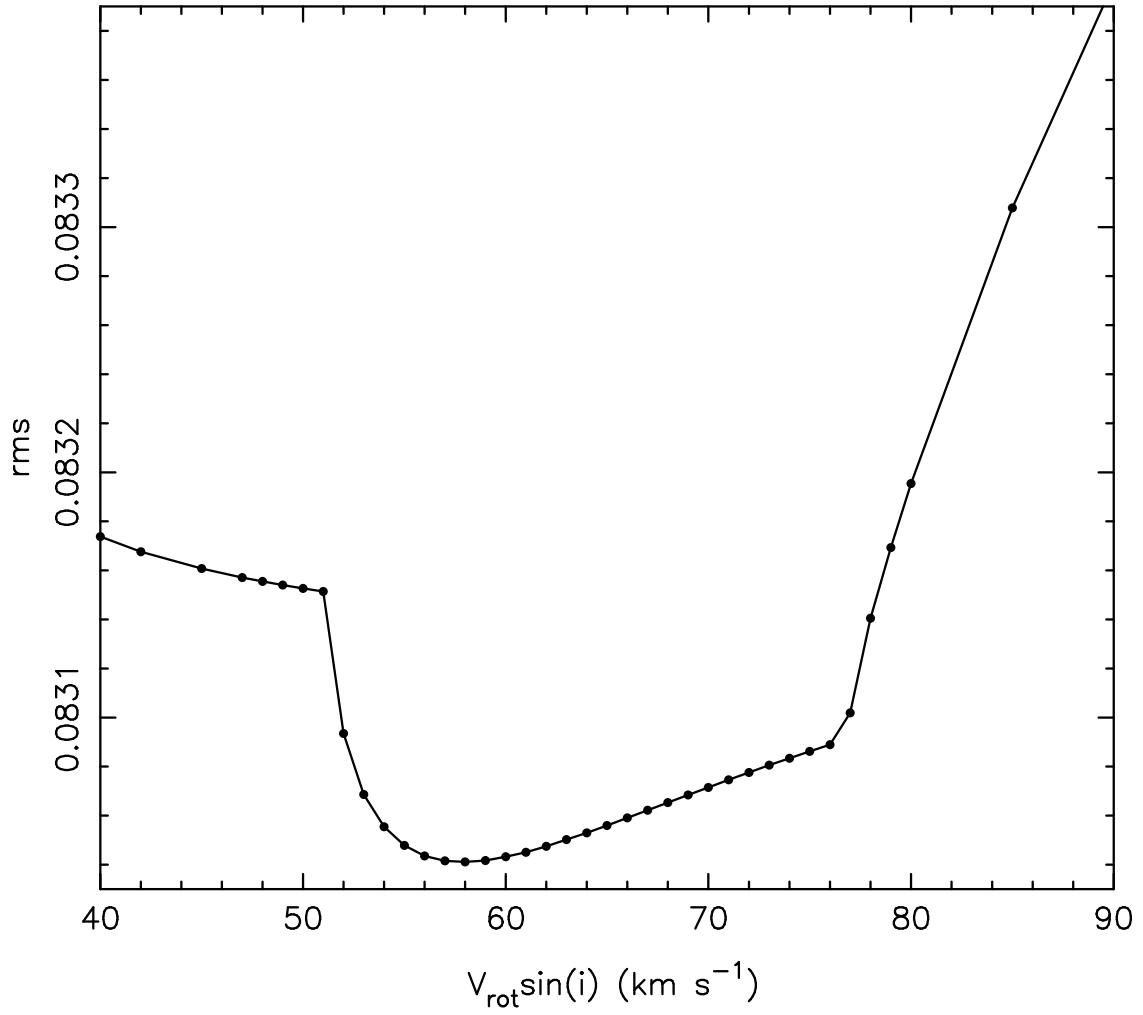


Fig. 7.— The rms value of the polynomial fits to the difference spectra as a function of the input projected rotational velocity of the template spectrum (which is the K3III star HD 181110). The minimum rms occurs when $V_{\text{rot}} \sin i = 57 \text{ km s}^{-1}$.

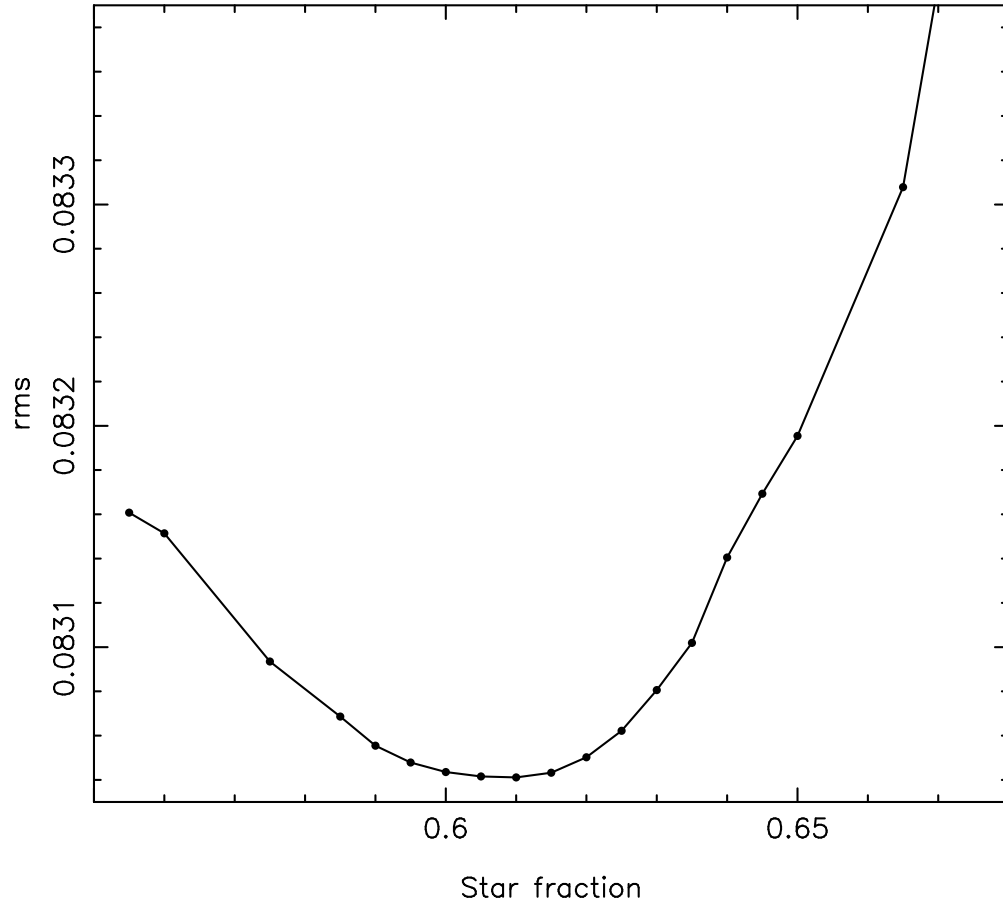


Fig. 8.— The rms value of the polynomial fits to the difference spectra as a function of the input star fraction, using the K3 III star HD 181110 as the template spectrum. We find a disk fraction of 0.39 at an effective wavelength of 6200 Å.

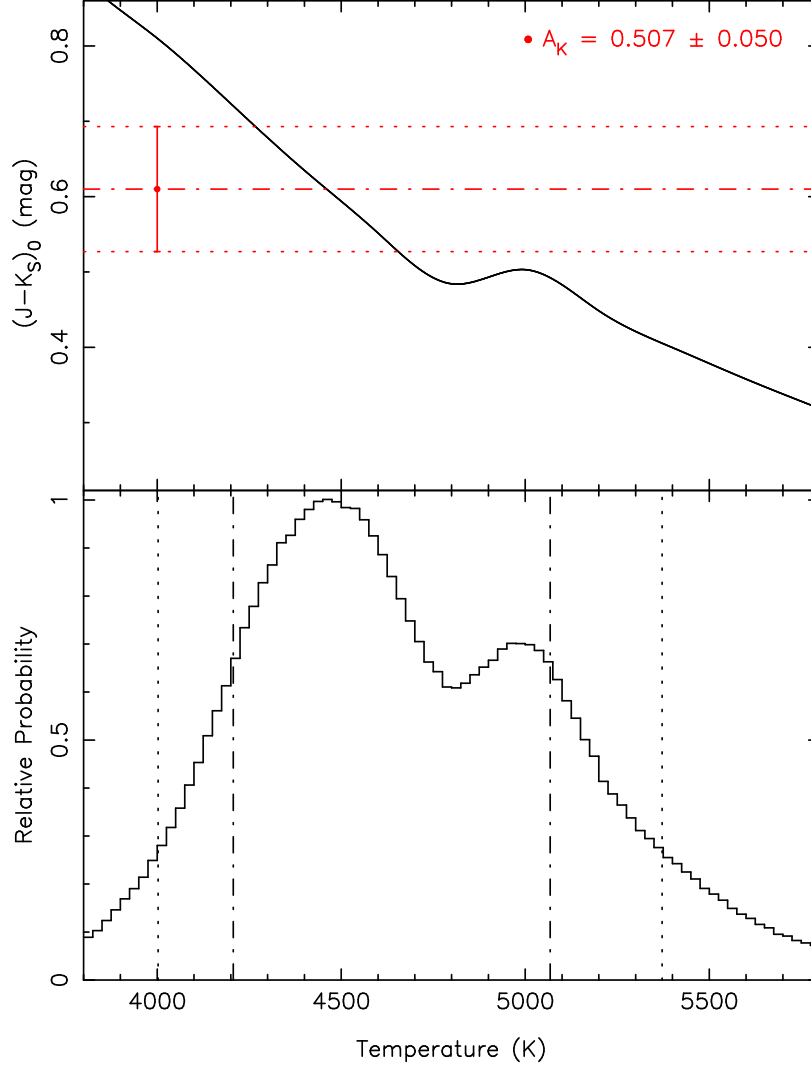


Fig. 9.— Top: The solid line gives the unreddened $J - K_S$ color of the secondary star as a function of temperature. The measured value of $(J - K_S)_0 = 0.610 \pm 0.071$ assuming $A_K = 0.507 \pm 0.050$ is indicated by the filled circle, and the 1σ range in the color is shown by the red horizontal dashed lines. Bottom: The distribution of the allowed temperatures derived from the observed color (assuming $A_K = 0.507 \pm 0.050$) is shown as the histogram. The 68% and 90% confidence intervals are denoted by the vertical dot-dashed lines and the dotted lines, respectively. Considering also the spectral type of the star, the most likely temperature is about $T_{\text{eff}} = 4450$ K.

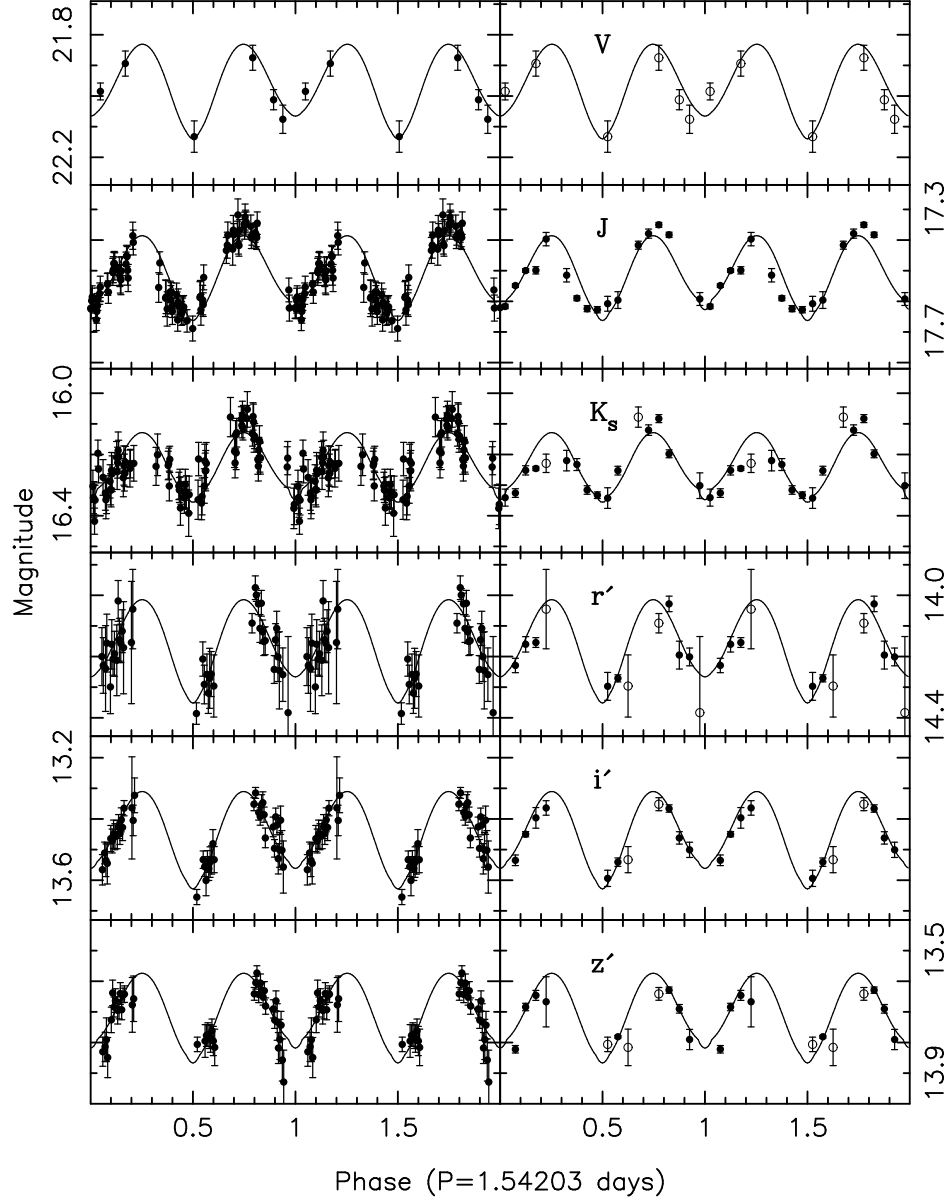


Fig. 10.— The left panels show the folded light curves in the V , J , K_S , and Sloan r' , i' , and z' filters and the best-fitting ellipsoidal models. The smoothed light curves shown in the right panels were made by computing the median magnitude within bins 0.05 phase units wide. Bins with a single point are indicated by an open circle. Note that only the V , J , and K_S magnitudes are calibrated to the standard scales.

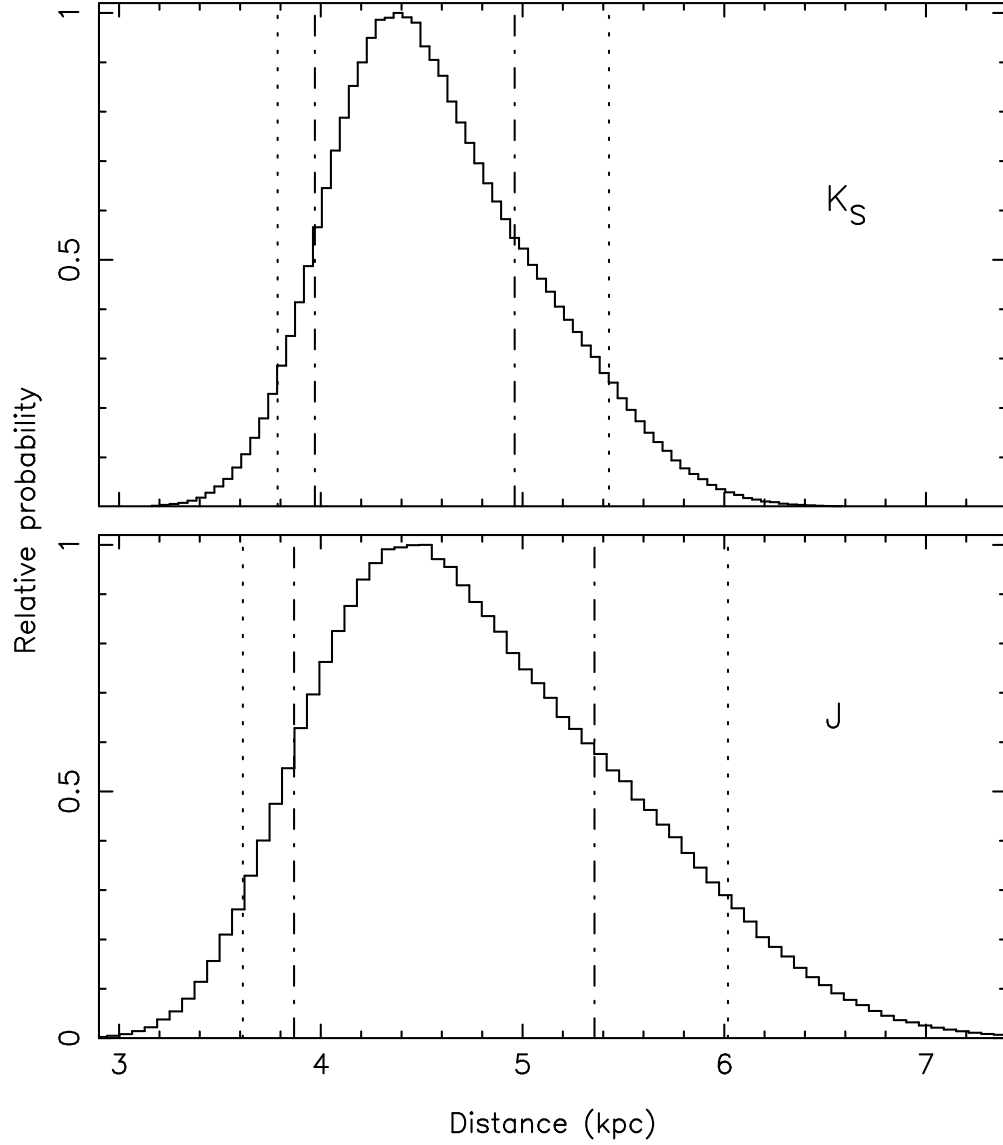


Fig. 11.— Top: This plot shows the probability distribution of the distance in kpc derived from a Monte Carlo simulation using the apparent K_S magnitude and extinction (see text). The 68% and 90% confidence intervals are denoted by the vertical dot-dashed lines and the dotted lines, respectively. The most likely distance is 4.38 kpc, with a 1σ range of $3.97 \leq d \leq 4.96$. Bottom: Same as the top, but with the distance computed using J -band measurements. The most likely value is 4.52 kpc, with a 1σ range of $3.87 \leq d \leq 5.36$.